SCIENTIFIC REPORTS

OPEN

Spin-polarized Second Harmonic Generation from the Antiferromagnetic CaCoSO Single Crystal

A. H. Reshak[1,2]

The spin-polarized second harmonic generation (SHG) of the recently synthesized CaCoSO single crystal is performed based on the calculated electronic band structure. The calculation reveals that the spin-up (↑) channel of CaCoSO possesses a direct energy gap (Γ^v-Γ^c) of about 2.187 eV, 1.187 eV (K^v-K^c) for the spin-down (↓) channel and an indirect gap (Γ^v-K^c) of about 0.4 eV for the spin-polarized CaCoSO single crystal. The linear optical properties obtained reveal that the recently synthesized crystal exhibits considerable anisotropy with negative uniaxial anisotropy and birefringence favor to enhance the SHG. We have calculated the three non-zero tensor components of the SHG and found the $\chi^{(2)}_{333}(\omega)$ is the dominat component, one with a large SHG of about ($d_{33} = 6.936$ pm/V at $\lambda = 1064$ nm), the half value of $KTiOPO_4$ (KTP). As the values of (↑)$|\chi^{(2)}_{333}(\omega)| <$ (↓)$|\chi^{(2)}_{333}(\omega)| <$ spin-polarized $|\chi^{(2)}_{333}(\omega)|$ are related to the values of the energy gap of (↑) 2.187 eV > (↓) 1.187 eV > spin-polarized gap 0.4 eV; therefore, a smaller energy gap gives better SHG performance. Furthermore, the microscopic first hyperpolarizability, β_{ijk}, is calculated.

A great effort has been made to synthesize novel nonlinear optical (NLO) crystals which are able to produce visible, UV and IR laser radiation at wavelengths that are presently inaccessible via conventional sources which have been in demand for several applications[1–4]. The NLO materials form a large group of semiconducting and dielectric materials with diverse optical, electrical, and structural properties. Some of these NLO materials appear to be promising candidates for optical frequency conversion applications in solid-state-based tunable laser systems[5–7]. These have potentially significant advantages over dye lasers because of their easier operation and the potential for more compact devices. Tunable frequency conversion in the mid-IR is based on optical parametric oscillators (OPO) using pump lasers in the near-IR. On the other hand, frequency doubling devices allow one to expand the range of powerful lasers in the far-IR. The transformation of frequencies within the wide spectral range of electromagnetic radiation (between 1–15 μm) for ultrafast lasers (from picoseconds up to femtoseconds) and large power densities can lead to significant progress in laser engineering. The method used for such frequency transformations is usually the generation of harmonic frequencies by employing high quality NLO crystals possessing large second optical susceptibilities[8,9]. In particular, the main method employed for frequency transformation is the second harmonic generation (SHG), where organic and inorganic crystals are now among the best[10,11]. Werake and Zhao[12] have reported the observation of the SHG in GaAs induced by pure spin current. Takas and Aitken[13] have presented the thermal analysis and SHG efficiency of α-Na_3PO_3S oxythiophosphate compound. Upon exposure to 1064 nm incident radiation, noncentrosymmetric α-Na3PO3S produces an SHG efficiency 200 times that of α-quartz and is nonphase-matchable (type 1). Wu et al.[14] have synthesized acentric $BaHgS_2$ by a conventional solid-state reaction method. It has been found that the powder of $BaHgS_2$ exhibits a large SHG response of about 6.5 times compared with that of reference $AgGaS_2$ at a fundamental wavelength (2.09 μm). Liu et al.[15] have synthesized a new oxychalcogenide, $BaGeOSe_2$ which contains acentric mixed-anion basic building units of GeO_2Se_2 tetrahedrons and $BaOSe_6$ polyhedrons. These GeO_2Se_2 tetrahedrons and $BaOSe_6$ polyhedrons are responsible for the large NLO response. Li et al.[16] reported that the combination of the highly electropositive alkali metal (Na) and Zn with a d^{10} electronic configuration into a crystal structure affords one new

[1]New Technologies - Research Centre, University of West Bohemia, Univerzitni 8, 306 14 Pilsen, Czech Republic. [2]School of Material Engineering, University Malaysia Perlis, 01007 Kangar, Perlis, Malaysia. Correspondence and requests for materials should be addressed to A.H.R. (email: maalidph@yahoo.co.uk)
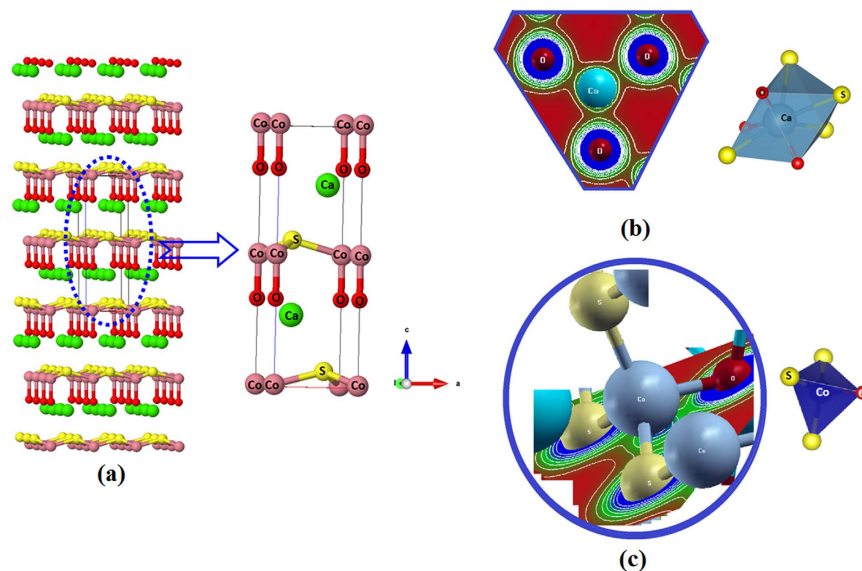
Figure 1. Crystal structure of the antiferromagnetic CaCoSO Single Crystal. (**b**) electron cloud in CaS$_4$O$_3$ (**c**) electron cloud in CoS$_3$O tetrahedron Co-O strong covalent bond.

IR NLO material, Na$_2$ZnGe$_2$S$_6$, which exhibits excellent properties including a wide transparent region, a large band gap, and especially a balance between the strong NLO coefficient (30 × KDP) and high LDT (6 × AgGaS2), which indicate a promising application in the IR region. A few years ago it was reported that AgGaX$_2$ (X = S, Se)[17–19] and ZnGeP$_2$[20,21] exhibit good SHG coefficients for application in the IR region. In the UV and visible regions, great achievements have been made by providing many excellent NLO materials like β-BaB2O4 (BBO), LiB3O5 (LBO) and KBe2BO3F2 (KBBF)[22–26]. Kang et al.[27] have designed two novel NLO carbonates KBeCO$_3$F and RbAlCO$_3$F$_2$ using the first-principles theory. The investigated crystals are structurally stable and possesses very large energy band gaps, and considerable optical anisotropy. They reported that KBeCO$_3$F and RbAlCO$_3$F$_2$ are very promising deep-UV NLO crystals alternative to KBBF. Liang et al.[28] have investigated the usage of metal sulfides with diamond-like (DL) for NLO applications in the mid-IR spectral region. The linear and NLO properties of the DL-metal sulfides are analyzed on the basis of first-principles calculations. It has been found that it is relatively easy to achieve good balance between the band gap and the NLO performance. Moreover, moderate birefringence Δn (~0.03–0.10) is crucial for practical mid-IR NLO applications. They reported that several metal sulfides with normal DL and defect DL structures, show excellent mid-IR NLO properties. These provide an useful information for the design and discovery of novel materials possesses good mid-IR NLO performance. Lin et al.[29] have reported that the *ab initio* approaches have the ability to accurately predict the optical properties in NLO crystals, and the developed analysis tools are very important to explore their intrinsic mechanism. This microscopic understanding is crucial for designing novel crystals with large NLO properties. It is expected that the first-principle approaches will deeply enhance the search efficiency and help the researchers to save resources in the exploration of novel NLO crystals with good performance.

Recently, the oxide chalcogenide compounds have become considerable candidates for several applications, for instance, as p-type transparent conductors[30–35]. Among these oxide chalcogenide compounds, the CaCoSO compound has been recently synthesized by Salter et al.[36]. It has been reported that the CaCoSO is isostructural with CaZnSO, BaCoSO and CaFeSO[36–40]. Since the newly synthesized CaCoSO crystallizes in non-centro-symmetry, this results in the loss of inversion symmetry, which in turn gives a considerable SHG. As the crystal structure of the CaCoSO single crystal has just been reported[36] and there is no further information regarding its linear and nonlinear optical properties, we think it would be worthwhile to perform a comprehensive theoretical calculation to calculate the spin-polarized linear, and nonlinear optical properties and the microscopic first hyperpolarizability. Moreover, it is important to highlight that there is no previous report on the spin-polarized nonlinear optical properties and the microscopic first hyperpolarizability for the CaCoSO. In the current work, we aim to find new materials without inversion symmetry and possessing considerable SHG, which have been in demand for many industrial, medical, biological and entertainment applications.

Density Functional Calculations

Very recently, Salter et al.[36] have synthesized CaCoSO in the form of a single crystal with a *P6$_3$mc* space group, cell parameters a = b = 3.7415(8) Å, c = 11.106(2) Å, V = 134.64(6) Å^3 and Z = 2, at room temperature[36]. Utilizing the reported x-ray diffraction data of CaCoSO[36], we performed comprehensive *ab-initio* calculations based on the full-potential method within the generalized gradient approximation (PBE-GGA) plus Hubbard Hamiltonian (U). In a step forward to gain accurate results, the experimental geometrical parameters[36] are optimized using PBE-GGA[41]. The optimized crystal structure of CaCoSO single crystal is shown in Fig. 1(a–c). The resulting geometrical parameters are used to perform the calculations employing the *ab-initio* LAPW+ lo full-potential
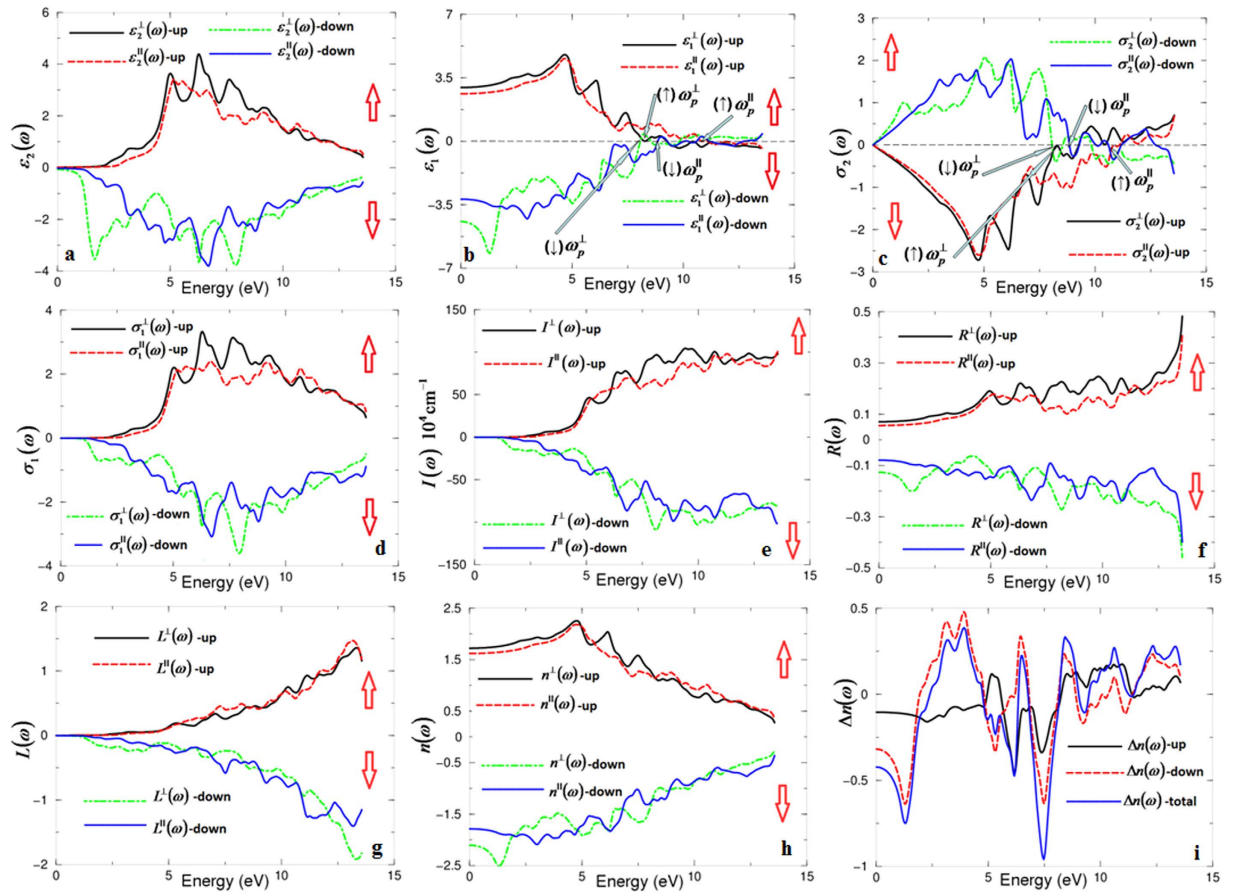
Figure 2. (**a**) Calculated $(\uparrow)\varepsilon_2^{\perp}(\omega)$ (dark solid curve-black color), $(\uparrow)\varepsilon_2^{\parallel}(\omega)$ (light long dashed curve-red color), $(\downarrow)\varepsilon_2^{\perp}(\omega)$ (light dotted dashed curve -green color) and $(\downarrow)\varepsilon_2^{\parallel}(\omega)$ (dark solid curve-blue color); (**b**) Calculated $(\uparrow)\varepsilon_1^{\perp}(\omega)$ (dark solid curve-black color), $(\uparrow)\varepsilon_1^{\parallel}(\omega)$ (light long dashed curve-red color), $(\downarrow)\varepsilon_1^{\perp}(\omega)$ (light dotted dashed curve -green color) and $(\downarrow)\varepsilon_1^{\parallel}(\omega)$ (dark solid curve-blue color); (**c**) Calculated $(\uparrow)\sigma_2^{\perp}(\omega)$ (dark solid curve-black color), $(\uparrow)\sigma_2^{II}(\omega)$ (light long dashed curve-red color), $(\downarrow)\sigma_2^{\perp}(\omega)$ (light dotted dashed curve -green color) and $(\downarrow)\sigma_2^{II}(\omega)$ (dark solid curve-blue color); (**d**) Calculated $(\uparrow)\sigma_1^{\perp}(\omega)$ (dark solid curve-black color), $(\uparrow)\sigma_1^{II}(\omega)$ (light long dashed curve-red color), $(\downarrow)\sigma_1^{\perp}(\omega)$ (light dotted dashed curve -green color) and $(\downarrow)\sigma_1^{II}(\omega)$ (dark solid curve-blue color); (**e**) Calculated $(\uparrow)I^{\perp}(\omega)$ (dark solid curve-black color), $(\uparrow)I^{II}(\omega)$ (light long dashed curve-red color), $(\downarrow)I^{\perp}(\omega)$ (light dotted dashed curve -green color) and $(\downarrow)I^{II}(\omega)$ (dark solid curve-blue color); (**f**) Calculated $(\uparrow)R^{\perp}(\omega)$ (dark solid curve-black color), $(\uparrow)R^{II}(\omega)$ (light long dashed curve-red color), $(\downarrow)R^{\perp}(\omega)$ (light dotted dashed curve -green color) and $(\downarrow)R^{II}(\omega)$ (dark solid curve-blue color); (**g**) Calculated $(\uparrow)L^{\perp}(\omega)$ (dark solid curve-black color), $(\uparrow)L^{II}(\omega)$ (light long dashed curve-red color), $(\downarrow)L^{\perp}(\omega)$ (light dotted dashed curve -green color) and $(\downarrow)L^{II}(\omega)$ (dark solid curve-blue color); (**h**) Calculated $(\uparrow)n^{\perp}(\omega)$ (dark solid curve-black color), $(\uparrow)n^{II}(\omega)$ (light long dashed curve-red color), $(\downarrow)n^{\perp}(\omega)$ (light dotted dashed curve -green color) and $(\downarrow)n^{II}(\omega)$ (dark solid curve-blue color); (**i**) Calculated $(\uparrow)\Delta n(\omega)$ (dark solid curve-black color), $(\downarrow)\Delta n(\omega)$ (light long dashed curve-red color) and total $\Delta n(\omega)$ (dark solid curve-blue color).

method utilizing the Wien2k code[42–44]. It is well known that for highly localized electrons, the Coulomb repulsion between the electrons in open shells should be taken into account; therefore, the Hubbard-like on-site repulsion should be added to the Kohn-Sham Hamiltonian. In the present work, we used the method of Anisimov *et al.*[45] and Liechtenstein *et al.*[46], where the Coulomb (U) and exchange (J) parameters are used. We applied the U on the 3*d* orbitals of the Co atom. Several U values are used to obtain a qualitative agreement with experimental data; we found 0.20 Ry is the optimal U value for Co-3*d*. In the current calculation, the self-consistency is obtained using 900 $\overrightarrow{k}$ points in the irreducible Brillouin zone (IBZ). The self-consistent calculations are converged since the total energy of the system is stable within 0.00001 Ry. The spin-polarized linear and nonlinear optical properties and the microscopic first hyperpolarizability are calculated using 25000 $\overrightarrow{k}$ points in the IBZ, as accurate calculations require a dense sampling of the BZ.

Results and Discussion

The spin-polarized linear optical properties of the antiferromagnetic CaCoSO are calculated based on the spin-polarized electronic band structure. The complex dielectric function consists of real and imaginary parts[47,48].

	CaCoSO	
	Spin-up	**Spin-down**
Eg (eV)	2.187	1.187
Spin-polarized Eg (eV)	0.4	
$\varepsilon_1^{\perp}(0)$	2.968	4.420
$\varepsilon_1^{\mathrm{II}}(0)$	2.621	3.184
$\delta\varepsilon$	−0.124	−0.325
$\omega_p^{\perp}(\omega)$	9.292	8.068
$\omega_p^{\mathrm{II}}(\omega)$	11.115	10.054
$n^{\perp}(0)$	1.722	2.102
$n^{\mathrm{II}}(0)$	1.619	1.784
$\Delta n(0)$	−0.103 ($\Delta n(\omega) = -0.125$ at $\lambda = 1064\,\mathrm{nm}$)	−0.318 ($\Delta n(\omega) = -0.595$ at $\lambda = 1064\,\mathrm{nm}$)
$\Delta n(0)$ total	−0.422 ($\Delta n(\omega) = -0.708$ at $\lambda = 1064\,\mathrm{nm}$)	

Table 1. The calculated energy band gap, $\varepsilon_1^{\perp}(0)$, $\varepsilon_1^{\mathrm{II}}(0)$, $\delta\varepsilon$, $\omega_p^{\perp}(\omega)$, $\omega_p^{\mathrm{II}}(\omega)$, $n^{\perp}(0)$, $n^{\mathrm{II}}(0)$ and $\Delta n(0)$.

For the hexagonal symmetry, the imaginary part consists of two tensor components: these are $\varepsilon_2^{\perp}(\omega)$ and $\varepsilon_2^{\mathrm{II}}(\omega)$. We have performed calculations for $\varepsilon_2^{\perp}(\omega)$ and $\varepsilon_2^{\mathrm{II}}(\omega)$ using the expression given elsewhere[47,48]. The calculated imaginary part for the spin-up (↑) and spin-down (↓) channels are shown in Fig. 2(a). Due to the fact that the spin-up channel has a different structure than that of the spin-down channel (see Fig. S1 Supplementary Materials), the resulting tensor components (↑)(↓)$\varepsilon_2^{\perp}(\omega)$ and (↑)(↓)$\varepsilon_2^{\mathrm{II}}(\omega)$ exhibit different spectral structures, following the allowed optical transitions between the occupied and unoccupied bands according to the selection rules. In order to identify the spectral structures of (↑)(↓)$\varepsilon_2^{\perp}(\omega)$ and (↑)(↓)$\varepsilon_2^{\mathrm{II}}(\omega)$, we need to look at the magnitude of the optical matrix elements for the spin-up and spin-down channels. The observed spectral structures in (↑)(↓)$\varepsilon_2^{\perp}(\omega)$ and (↑)(↓)$\varepsilon_2^{\mathrm{II}}(\omega)$ would correspond to those transitions that have large optical matrix elements. It has been noted that the fundamental absorption edge for (↑)$\varepsilon_2^{\perp}(\omega)$ and (↑)$\varepsilon_2^{\mathrm{II}}(\omega)$ is situated at about 2.187 eV, whereas for (↓)$\varepsilon_2^{\perp}(\omega)$ and (↓)$\varepsilon_2^{\mathrm{II}}(\omega)$ it is located at around 1.187 eV, which confirms that the spin-up channel possesses an energy band gap larger that that of the spin-down channel (see Fig. S1 Supplementary Materials). We should emphasize that the broadening is taken to be 0.1 eV, which is traditional for oxide crystals and is typical of the experimental accuracy. In the spin-up channel the fundamental absorption edge occurs due to the optical transition from Co-3p/3d, S-3p, and O-2p bands of the VBs to Ca-s/p, Co-4s/3p and O-2s bands of the CBs, while in the spin-down channel it occurs between Co-3p/3d, O-2p, S-3p VBs and Co-3p/3d, Ca-3p, O-2p, S-3p CBs. The main structure which is confined between 5.0 eV and 10.0 eV occurs due to the optical transitions between Ca-4s/3p, Co-4s/3p/3d, O-2s/2p, S-3s/3p VBs and Ca-4s/3p, O-2s CBs in the spin-up channel. Whereas in the spin-down channel it is formed due to the transitions from Ca-4s/3p, Co-4s/3p, O-2s/2p, S-3s/3p VBs to Ca-4s/3p, Co-4s/3p/3d, O-2s CBs.

With the aid of the Kramers-Kronig relations[47,48], the real parts of the optical dielectric function can be obtained from the imaginary part. Figure 2(b) illustrates the spectral features of (↑)(↓)$\varepsilon_1^{\perp}(\omega)$ and (↑)(↓)$\varepsilon_1^{\mathrm{II}}(\omega)$. The calculated values of (↑)(↓)$\varepsilon_1^{\perp}(\omega)$ and (↑)(↓)$\varepsilon_1^{\mathrm{II}}(0)$ at the static limit are listed at Table 1, which shows that the values of (↓)$\varepsilon_1^{\perp}(\omega)$ and (↓)$\varepsilon_1^{\mathrm{II}}(0)$ are grater than those of (↑)$\varepsilon_1^{\perp}(\omega)$ and (↑)$\varepsilon_1^{\mathrm{II}}(0)$. This confirms that the spin-down channel possesses an energy band gap smaller that that of the spin-up channel, following the Penn model $\varepsilon(0) \approx 1 + (\hbar\omega_p/E_g)^2$ [49], which shows that $\varepsilon(0)$ is inversely proportional to the energy band gap. Furthermore, from the spectral structures of (↑)(↓)$\varepsilon_1^{\perp}(\omega)$ and (↑)(↓)$\varepsilon_1^{\mathrm{II}}(\omega)$, we can obtain the values of the uniaxial anisotropy ($\delta\varepsilon$). These values are listed in Table 1 and show that the CaCoSO possesses negative $\delta\varepsilon$ for both channels. The plasma frequency can be obtained at the intersection points where (↑)(↓)$\varepsilon_1^{\perp}(\omega)$ and (↑)(↓)$\varepsilon_1^{\mathrm{II}}(\omega)$ cross the energy axis (x-axis), as shown in Fig. 2(b). The calculated values of (↑)(↓)$\omega_p^{\perp}(\omega)$ and (↑)(↓)$\omega_p^{\mathrm{II}}(\omega)$ are listed in Table 1; these are the values of the plasmon maximum, which are the most intensive features in the optical spectrum.

From the calculated (↑)(↓)$\varepsilon_2^{\perp}(\omega)$, (↑)(↓)$\varepsilon_2^{\mathrm{II}}(\omega)$, (↑)(↓)$\varepsilon_1^{\perp}(\omega)$ and (↑)(↓)$\varepsilon_1^{\mathrm{II}}(\omega)$, we can obtain (↑)(↓)$\sigma_2^{\perp}(\omega)$, (↑)(↓)$\sigma_2^{\mathrm{II}}(\omega)$, (↑)(↓)$\sigma_1^{\perp}(\omega)$ and (↑)(↓)$\sigma_1^{\mathrm{II}}(\omega)$, as shown in Fig. 2(c,d). The optical conductivity is directly related to the energy band structure of solids[50]; therefore, deep insight into the electronic structure of the materials can be further obtained from the optical conductivity. Furthermore, from the imaginary part of the optical conductivity, the (↑)(↓)$\omega_p^{\perp}(\omega)$ and (↑)(↓)$\omega_p^{\mathrm{II}}(\omega)$ values can be obtained (Table 1).

Figure 2(e) illustrates the absorption coefficients of CaCoSO for the spin-up and spin-down channels. The fundamental absorption edge of the spin-up channel occurs at 2.187 eV, whereas it is 1.187 eV for the spin-down channel, which reveals that the absorption edge of the spin-down is smaller than that of the spin-up, confirming our previous observation at Fig. 2(a).

The reflectivity spectra (Fig. 2f) reveal that the CaCoSO possesses low reflectivity at the low energy range and the highest reflectivity at around 13.0 eV, which represents the lossless region. To support this statement the loss function is calculated and presented in Fig. 2(g). The refractive indices are very important quantities to determine the phase matching conditions which are necessary for the second harmonic generation. The spin-up/down refractive indices of the CaCoSO single crystal are calculated and presented in Fig. 2(h). From the parallel
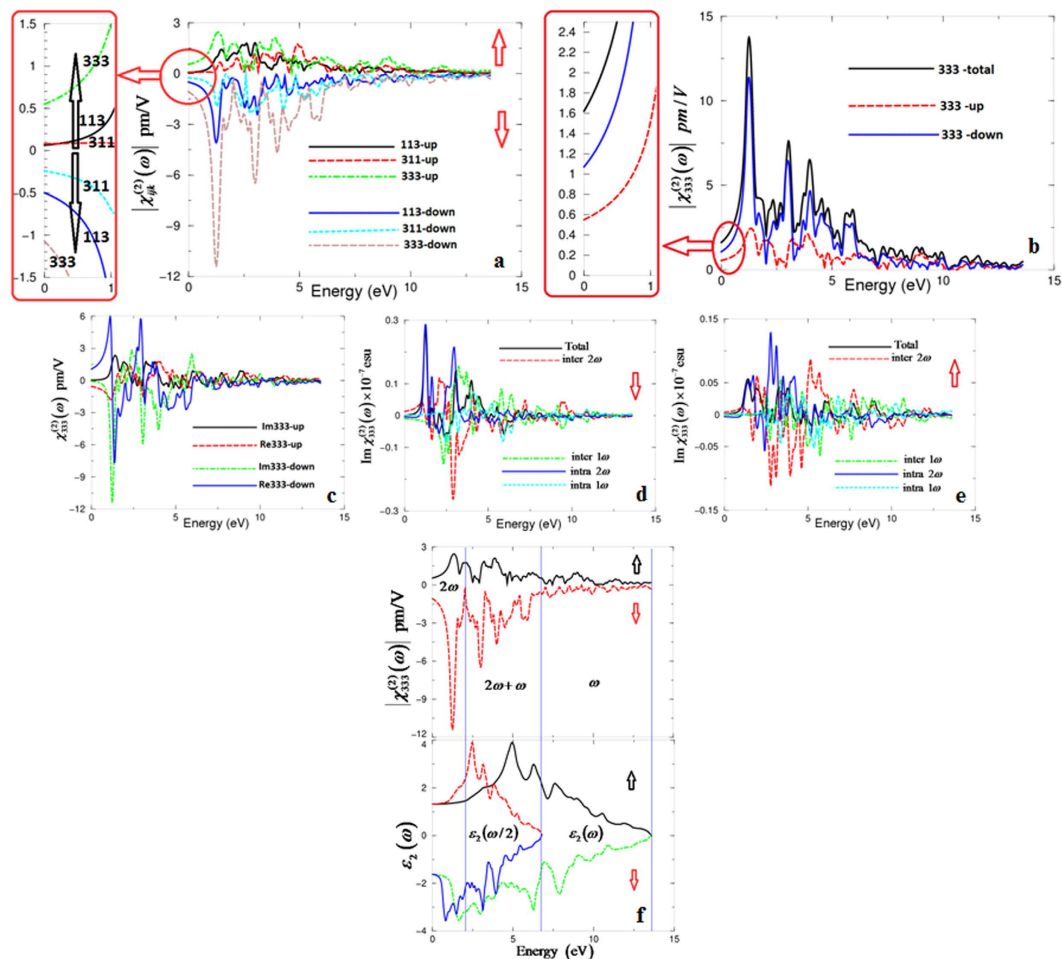
Figure 3. (**a**) Calculated $(\uparrow)(\downarrow)|\chi_{ijk}^{(2)}(\omega)|$ for the three tensor components of CaCoSO single crystal; (**b**) Calculated $(\uparrow)(\downarrow)|\chi_{333}^{(2)}(\omega)|$ and the total $|\chi_{333}^{(2)}(\omega)|$ the dominate tensor component of CaCoSO single crystal; (**c**) Calculated $(\uparrow)(\downarrow)$ of the imaginary and real parts of $\chi_{333}^{(2)}(\omega)$ the dominate tensor component of CaCoSO single crystal; (**d**) Calculated $(\uparrow)$ of the imaginary part of $\chi_{333}^{(2)}(\omega)$ spectrum (dark solid curve-black color) along with the intra $(2\omega)/(1\omega)$ (light solid curve-blue color)/(light dashed doted curve-cyan color) and inter $(2\omega)/(1\omega)$ (light long dashed curve-red color)/(light doted curve-green color) -band contributions, here all Im$\chi_{333}^{(2)}(\omega)$ are multiplied by 10^{-7}, in esu units; (**e**) Calculated $(\downarrow)$ of the imaginary part of $\chi_{333}^{(2)}(\omega)$ spectrum (dark solid curve-black color) along with the intra $(2\omega)/(1\omega)$ (light solid curve-blue color)/(light dashed doted curve-cyan color) and inter $(2\omega)/(1\omega)$ (light long dashed curve-red color)/(light doted curve-green color) -band contributions, here all Im$\chi_{333}^{(2)}(\omega)$ are multiplied by 10^{-7}, in esu units; (**f**) -*upper panel*- Calculated $(\uparrow)|\chi_{333}^{(2)}(\omega)|$ (dark solid curve-black color) and $(\downarrow)|\chi_{333}^{(2)}(\omega)|$ (light long dashed curve-red color); -*lower panel*- Calculated $(\uparrow)\varepsilon_2(\omega)$ (dark solid curve-black color); Calculated $(\uparrow)\varepsilon_2(\omega/2)$ (dark dashed curve-red color); Calculated $(\downarrow)\varepsilon_2(\omega/2)$ (light dotted dashed curve -green color); Calculated $(\downarrow)\varepsilon_2(\omega/2)$ (dark solid curve-blue color).

and perpendicular tensor components of the refractive indices, the birefringence can be obtained. The calculated spin-up/down and spin-polarized birefringence are presented in Fig. 2(i). The calculated values of the birefringence at the static limit and at the wavelength 1064 nm are listed at Table 1. It is clear that the CaCoSO single crystal exhibits relatively large birefringence. The electron clouds of the CaO_3S_4 and CoS_3O (Fig. 1b,c) exhibit a planar shape with conjugated electron orbitals, which make the CoS_3O groups the main source of the large birefringence in CaCoSO. It is well known that the birefringence determines partly whether an NLO material has the value of study[51]. It is clear that there is a considerable anisotropy between the two tensor components of the optical properties. The high electron density configuration and strong anisotropy for Co-S and Co-O indicate the main contribution of CoS_3O to the optical anisotropy. The optical anisotropy is a favor to enhance the SHG.

Furthermore, we have calculated the spin-up $(\uparrow)$ and spin-down $(\downarrow)$ and the spin-polarized second harmonic generation for the CaCoSO single crystal. The formalisms which are used to calculate the complex nonlinear optical are presented elsewhere[52–54]. The investigated single crystal possesses three non-zero tensor components. These are 113, 311 and 333; only one of these tensor components is the most intensive one and acts as the dominant one. From the calculated $(\uparrow)(\downarrow)|\chi_{ijk}^{(2)}(\omega)|$ (Fig. 3a), we can notice that the $(\uparrow)(\downarrow)|\chi_{333}^{(2)}(\omega)|$ is the most intensive among the others; therefore, $|\chi_{333}^{(2)}(\omega)|$ is the dominant due to the crystal's symmetry. Figure 3(b) illustrates the

	Spin-up		Spin-dn		Spin-up at $\lambda = 1064$ nm		Spin-dn at $\lambda = 1064$ nm	
	$\chi_{ijk}^{(2)}(0)$	$d_{ijk} = 0.5\chi_{ijk}^{(2)}(0)$	$\chi_{ijk}^{(2)}(0)$	$d_{ijk} = 0.5\chi_{ijk}^{(2)}(0)$	$\chi_{ijk}^{(2)}(0)$	$d_{ijk} = 0.5\chi_{ijk}^{(2)}(\omega)$	$\chi_{ijk}^{(2)}(0)$	$d_{ijk} = 0.5\chi_{ijk}^{(2)}(\omega)$
$\lvert\chi_{113}^{(2)}(\omega)\rvert$	0.064	$d_{15} = 0.032$	0.499	$d_{15} = 0.249$	0.783	$d_{15} = 0.391$	3.656	$d_{15} = 1.828$
$\lvert\chi_{311}^{(2)}(\omega)\rvert$	0.079	$d_{31} = 0.039$	0.240	$d_{31} = 0.120$	0.126	$d_{31} = 0.063$	1.270	$d_{31} = 0.635$
$\lvert\chi_{333}^{(2)}(\omega)\rvert$	0.549	$d_{33} = 0.275$	1.071	$d_{33} = 0.535$	2.167	$d_{33} = 1.083$	10.433	$d_{33} = 5.216$
Spin-polarized $\lvert\chi_{333}^{(2)}(\omega)\rvert$	1.628 ($d_{33} = 0.814$)				13.872 ($d_{33} = 6.936$)			
β_{333}	0.0803×10^{-30} esu		0.1563×10^{-30} esu		0.3225×10^{-30} esu		1.5867×10^{-30} esu	
Spin-polarized β_{333}	0.2317×10^{-30} esu				1.9215×10^{-30} esu			

Table 2. Calculated spin-polarized $\lvert\chi_{ijk}^{(2)}(\omega)\rvert$ and β_{ijk} of CaCoSO, in pm/V at static limit and at $\lambda = 1064$ nm. Where $1\,\text{pm/V} = 2.387 \times 10^{-9}$ esu.

dominant tensor component for the spin-up, spin-down and the spin-polarized $\lvert\chi_{333}^{(2)}(\omega)\rvert$ for the CaCoSO single crystal. The SHG values of the three tensor components are listed in Table 2, which shows that the investigated crystal possesses a large SHG of about 1.628 pm/V at the static limit and 13.872 pm/V ($d_{33} = 6.936$ pm/V) at $\lambda = 1064$ nm. The obtained value of the SHG at $\lambda = 1064$ nm is about the half value of the well-known NLO crystal $KTiOPO_4$ (KTP)[55]. Following Table 2, the $(\uparrow)\lvert\chi_{333}^{(2)}(\omega)\rvert < (\downarrow)\lvert\chi_{333}^{(2)}(\omega)\rvert <$ spin-polarized $\lvert\chi_{333}^{(2)}(\omega)\rvert$ is related to the value of the energy gap ($\uparrow$) 2.187 eV > ($\downarrow$) 1.187 eV > spin-polarized gap 0.4 eV; therefore, we can see that our finding is supported by the statement: a smaller energy gap gives better SHG performance.

The dominant tensor component $\chi_{333}^{(2)}(\omega)$ consists of imaginary and real parts as shown in Fig. 3(c) for the spin-up, spin-down channels. The imaginary and real parts further consist of $2\omega/\omega$ inter-/intra-band contributions as shown in Fig. 3(d,e). In order to understand the origin of the spectral features of the dominant tensor component $\lvert\chi_{333}^{(2)}(\omega)\rvert$, the imaginary part of the dielectric function as a function of $\omega/2$ and ω is associated with $\lvert\chi_{333}^{(2)}(\omega)\rvert$, as shown in Fig. 3(f). This clearly shows that the structure below the half energy gap (1.093 eV($\uparrow$), 0.593 eV($\downarrow$)) is associated with 2ω resonance, whereas the structure above the fundamental energy gap (2.187 eV ($\uparrow$), 1.187 eV($\downarrow$)) is associated with interference between 2ω and ω resonances and the tail is mainly due to ω resonance. The values of the microscopic first hyperpolarizability, β_{ijk}[56,57], vector component along the dipole moment direction for the dominate tensor component are calculated at the static limit and at $\lambda = 1064$ nm, as shown in Table 2.

Conclusions

Based on the experimental crystallographic data of the recently synthesized CaCoSO single crystal, the spin-polarized SHG is calculated and the origin of the large SHG is discussed in detail. It has been found that the spin-up channel of the CaCoSO single crystal possesses direct energy (Γ^v-Γ^c) of about 2.187 eV, 1.187 eV (K^v-K^c) for the spin-down channel and an indirect gap (Γ^v-K^c) of about 0.4 eV for the spin-polarized CaCoSO single crystal. The linear optical properties reveal that the recently synthesized crystal exhibits considerable anisotropy with negative uniaxial anisotropy and birefringence favor to enhance the SHG. It is clear that CaCoSO single crystal exhibits relatively large birefringence. The electron clouds of the CaO_3S_4 and CoS_3O groups exhibit a planar shape with conjugated electron orbitals, which make the CaO_3S_4 and CoS_3O groups the main source of the large birefringence in CaCoSO. It is well known that the birefringence determines partly whether an NLO material has the value of study. The high electron density configuration and strong anisotropy for Co-S and Co-O indicate the main contribution of CaO_3S_4 and CoS_3O to the optical anisotropy. The optical anisotropy is a favor to enhance the SHG. We have calculated the three non-zero tensor components of the SHG and found the $\chi_{333}^{(2)}(\omega)$ is the dominant one, with a large SHG of about ($d_{33} = 6.936$ pm/V at $\lambda = 1064$ nm), the half value of the well-known NLO crystal $KTiOPO_4$ (KTP). The $(\uparrow)\lvert\chi_{333}^{(2)}(\omega)\rvert < (\downarrow)\lvert\chi_{333}^{(2)}(\omega)\rvert <$ spin-polarized $\lvert\chi_{333}^{(2)}(\omega)\rvert$ is related to the value of the energy gap of the ($\uparrow$) 2.187 eV > ($\downarrow$) 1.187 eV > spin-polarized gap 0.4 eV; therefore, we can see that our finding is supported by the statement: a smaller energy gap gives better SHG performance. Furthermore, the values of the microscopic first hyperpolarizability, β_{ijk}, for the dominant tensor component is calculated at the static limit and at $\lambda = 1064$ nm.

References

1. Li, D. *et al.* Theoretical perspective of the lone pair activity influence on band gap and SHG response of lead borates. *RSC Adv.* **97**, 79882−79887 (2015).
2. Dong, W. T. *et al.* Crystal Growth, Structure, and Properties of New Nonlinear Optical Materials: K2Ln(NO3)5·2H2O (Ln = La, Ce, Pr, Nd, Sm). *J. Solid State Chem.* **148**, 302−307 (1999).
3. Chang, L. *et al.* A Nitrate Nonlinear Optical Crystal Pb16(OH)16(NO3)16 with a Large Second-Harmonic Generation Response. *Inorg. Chem.* **53**, 3320−3325 (2014).
4. Reshak, A. H. *et al.* Dispersion of linear and non-linear optical susceptibilities for amino acid 2-aminopropanoic CH3CH(NH2) COOH single crystals: experimental and theoretical investigations. *J. Mater. Chem.* **21**, 17219 (2011).
5. Chen, C. *et al.* New Development of Nonlinear Optical Crystals for The Ultraviolet Region with Molecular Engineering Approach. *J. Appl. Phys.* **77**, 2268–2272 (1995).
6. Lekse, J. W. *et al.* Second-Harmonic Generation and Crystal Structure of the Diamond-like Semiconductors Li2CdGeS4 and Li2CdSnS4. *Inorg. Chem.* **48**, 7516–7518 (2009).
7. Brant, J. A. *et al.* Li2CdGeS4, A Diamond-Like Semiconductor with Strong Second-Order Optical Nonlinearity in the Infrared and Exceptional Laser Damage Threshold. *Chem. Mater.* **26**, 3045−3048 (2014).
8. Majchrowski, A. *et al.* β-BaTeMo2O9 microcrystals as promising optically operated materials. *J. Mater. Sci.* **48**, 5938–5945 (2013).
9. Gao, Z. L., Wu, Q., Liu, X. T., Sun, Y. X. & Tao, X. T. Biaxial crystal α-BaTeMo2O9: theory study of large birefringence and wide-band polarized prisms design. *Opt. Express.* **23**, 3851 (2015).

10. Zhang, J., Zhang, Z., Sun, Y., Zhang, C. & Tao, X. Bulk crystal growth and characterization of a new polar polymorph of $BaTeMo_2O_9$: α-$BaTeMo_2O_9$. *CrystEngComm.* **13,** 6985 (2011).
11. Simpson, H. J. & Marsh, R. E. The crystal structure of L-alanine. *Acta Cryst.* **20,** 550 (1966).
12. Werake, L. K. & Zhao, H. Observation of second-harmonic generation induced by pure spin currents. *Nature Physic.* **6,** 875–878 (2010).
13. Nathan, J. & Takas Jennifer, A. Aitken. Phase Transitions and Second-Harmonic Generation in Sodium Monothiophosphate. *Inorg. Chem.* **45,** 2779–2781 (2006).
14. Wu, K., Su, X., Pan, S. & Yang, Z. Synthesis and Characterization of Mid-Infrared Transparency Compounds: Acentric $BaHgS_2$ and Centric $Ba_8Hg_4S_5Se_7$. *Inorg. Chem.* **54,** 2772−2779 (2015).
15. Bin-Wen, L. *et al.* Oxychalcogenide $BaGeOSe_2$: Highly Distorted Mixed-Anion Building Units Leading to A Large Second Harmonic Generation Response. *Chem. Mater.* **27(24),** 8189–8192 (2015).
16. Li, G., Wu, K., Liu, Q., Yang, Z. & Pan, S. $Na_2ZnGe_2S_6$: A New Infrared Nonlinear Optical Material with Good Balance between Large Second-Harmonic Generation Response and High Laser Damage Threshold. *J. Am. Chem. Soc.* **138(23),** 7422–7428 (2016).
17. Okorogu, A. O. *et al.* Tunable middle infrared downconversion in GaSe and $AgGaS_2$. *Opt. Commun.* **155,** 307–312 (1998).
18. Boyd, G., Kasper, H. & McFee, J. Linear and nonlinear optical properties of $AgGaS_2$, $CuGaS_2$, and $CuInS_2$, and theory of the wedge technique for the measurement of nonlinear coefficients. *IEEE Journal of Quantum Electronics.* **7(12),** 563–573 (1971).
19. Dmitriev, V. G., Gurzadyan, G. G. & Nikogosyan, D. N. *Handbook of Nonlinear Optical Crystals* 3rd ed. Springer, New York (1999).
20. Jackson, A. G., Ohmer, M. C. & LeClair, S. R. Relationship of the second order nonlinear optical coefficient to energy gap in inorganic non-centrosymmetric crystals. *Infrared Physics & Technology.* **38,** 233–244 (1997).
21. Boyd, G. D., Buehler, E. & Storz, F. G. Linear and nonlinear optical properties of $ZnGeP2$ and CdSe. *Applied Physics Letters.* **18(7),** 301–304 (1971).
22. Kato, K. Parametric oscillation at 3.2 p.m. in KTP pumped at 1.064 pm. *IEEE J. Quantum Electron.* **27,** 1137–1140 (1991).
23. Boyd, G. D., Miller, R. C., Nassau, K., Bond, W. L. & Savage, A. LiNbO3: An efficient phase matchable nonlinear optical material. *Appl. Phys. Lett.* **5,** 234 (1964).
24. Chen, C. T. *et al.* New nonlinear-optical crystal: LiB_3O_5. *J. Opt. Soc. Am. B.* **6,** 616 –621 (1989).
25. Mori, Y., Kuroda, I., Nakajima, S., Sasaki, T. & Nakai, S. New nonlinear optical crystal: Cesium lithium borate. *Appl. Phys. Lett.* **67,** 1818–1820 (1995).
26. Xia, Y. N., Chen, C. T., Tang, D. Y. & Wu, B. C. New nonlinear-optical crystals for UV and VUV harmonic-generation. *Adv. Mater.* **7,** 79–81 (1995).
27. Kang, L., Lin, Z., Qin, J. & Chen, C. Two novel nonlinear optical carbonates in the deep-ultraviolet region: $KBeCO_3F$ and $RbAlCO_3F_2$. *Sci. Rep.* **3,** 1366 (2013).
28. Liang, F., Kang, L., Lin, Z., Wu, Y. & Chen, C. Analysis and prediction of mid-IR nonlinear optical metal sulfides with diamond-like structures. *Coordination Chemistry Reviews* **333,** 57–70 (2017).
29. Lin, Z., Jiang, X., Kang, L., Gong, P., Luo, S. & Lee, M.-H. First-principles materials applications and design of nonlinear optical crystals. *J. Phys. D: Appl. Phys.* **47,** 253001(2014).
30. Ueda, K., Inoue, S., Hirose, S., Kawazoe, H. & Hosono, H. Transparent p-type semiconductor: LaCuOS layered oxysulfide. *Appl. Phys. Lett.* **77,** 2701−2703 (2000).
31. Kamihara, Y., Watanabe, T., Hirano, M. & Hosono, H. J. Iron-Based Layered Superconductor $La[O_{1−x}F_x]FeAs$ ($x = 0.05−0.12$) with $T_c = 26\,K$. *Am. Chem. Soc.* **130,** 3296−3297 (2008).
32. Clarke, S. J. *et al.* Structures, Physical Properties, and Chemistry of Layered Oxychalcogenides and Oxypnictides. *Inorg. Chem.* **47,** 8473−8486 (2008).
33. Petrova, S. A. *et al.* Crystal Structure of Zinc Calcium Oxysulfide. *Dokl. Chem.* **393,** 255−258 (2003).
34. Sambrook, T., Smura, C. F., Clarke, S. J., Ok, K. M. & Halasyamani, P. S. Structure and Physical Properties of the Polar Oxysulfide CaZnOS. *Inorg. Chem.* **46,** 2571−2574 (2007).
35. Broadley, S., Gál, Z. A., Corà, F., Smura, C. F. & Clarke, S. J. Vertex-Linked ZnO_2S_2 Tetrahedra in the Oxysulfide BaZnOS: a New Coordination Environment for Zinc in a Condensed Solid. *Inorg. Chem.* **44,** 9092−9096 (2005).
36. Salter, E. J., Blandy, J. N. & Clarke, S. J. Crystal and Magnetic Structures of the Oxide Sulfides CaCoSO and BaCoSO. *Inorg. Chem.* **55,** 1697–1701 (2016).
37. Selivanov, E. N. *et al.* Composition, Structure, and Thermal Expansion of $Ca_3Fe_4S_3O_6$ and CaFeSO. *Inorg. Mater.* **40,** 845−850 (2004).
38. Delacotte, C. *et al.* Magnetodielectric Effect in Crystals of the Noncentrosymmetric CaOFeS at Low Temperature. *Inorg. Chem.* **54,** 6560−6565 (2015).
39. Jin, S. F. *et al.* Two-dimensional magnetic correlations and partial long-range order in geometrically frustrated CaOFeS with triangle lattice of Fe ions. *Phys. Rev. B: Condens. Mater. Phys.* **91,** 094420 (2015).
40. Valldor, M. *et al.* Synthesis and Characterization of Ba[CoSO]: Magnetic Complexity in the Presence of Chalcogen Ordering. *Chem. - Eur. J.* **21,** 10821−10828 (2015).
41. Perdew, J. P., Burke, S. & Ernzerhof, M. Generalized Gradient Approximation Made Simple. *Phys. Rev. Lett.* **77,** 3865 (1996).
42. Blaha P., Schwarz K., Madsen G. K. H., Kvasnicka D. & Luitz J. WIEN2k, An augmented plane wave plus local orbitals program for calculating crystal properties, Vienna University of Technology, Austria (2001).
43. Andersen, O. K. Linear methods in band theory. *Phys. Rev. B* **12,** 3060 (1975).
44. Perdew, J. P. & Wang Y. Accurate and simple analytic representation of the electron-gas correlation energy. *Phys. Rev. B* **45,** 13244 (1992).
45. Anisimov, V. I., Solvyev, I. V., Korotin, M. A., Czyzyk, M. T. & Sawatzky, C. A. Density-functional theory and NiO photoemission spectra. *Phys. Rev. B* **48,** 16929 (1993).
46. Liechtenstein, A. I., Anisimov, V. I. & Zaanen, J. Density-functional theory and strong interactions: Orbital ordering in Mott-Hubbard insulators. *J. Phys. Rev. B.* **52,** R5467 (1995).
47. Bassani, F. & Parravicini, G. P. *Electronic States and Optical Transitions In Solids* Pergamon Press Ltd., Oxford, p149–154 (1975).
48. Ambrosch-Draxl, C. & Sofo, J. O. Linear optical properties of solids within the full-potential linearized augmented planewave method. *Computer Physics Communications.* **175,** 1–14 (2006).
49. Penn, D. R. Wave-Number-Dependent Dielectric Function of Semiconductors. *Phys. Rev. B.* **128,** 2093 (1962).
50. Dresselhaus, M. S. Solid State Physics Part II Optical Properties of Solids, vol. 6 (2001).
51. Bian, Q. *et al.* First Principle Assisted Prediction of the Birefringence Values of Functional Inorganic Borate Materials. *J. Phys. Chem. C.* **118(44),** 25651–25657 (2014).
52. Sharma, S. & Ambrosch-Draxl, C. Second-Harmonic Optical Response from First Principles. *Physica Scripta T.* **109,** 128 (2004).
53. Rashkeev, S. N., Lambrecht, W. R. L. & Segall, B. Efficient ab initio method for the calculation of frequency-dependent second-order optical response in semiconductors. *Phys. Rev. B.* **57,** 3905 (1998).
54. Aspnes, D. E. Energy-Band Theory of the Second-Order Nonlinear Optical. *Phys. Rev. B.* **6,** 4648 (1972).
55. Reshak, A. H., Kityk, I. V. & Auluck, S. Investigation of the Linear and Nonlinear Optical Susceptibilities of $KTiOPO_4$ Single Crystals: Theory and Experiment. *J. Phys. Chem. B.* **114,** 16705–16712 (2010).
56. Boyd, R. Y. *Principles of Nonlinear Optics* NY, Academic Press, 420 p (1982).
57. Boyd, R. W. Nonlinear optics, third edition, Academic Press is an imprint of Elsevier, ISBN:978-0-12-369470-6 (2008).

Acknowledgements

Author Contributions

A.H. Reshak, as a professor with PhD in physics has performed the calculations, analyzing and discussing the results and writing the manuscript.

Additional Information

Supplementary information accompanies this paper at http://www.nature.com/srep

Competing Interests: The authors declare no competing financial interests.

How to cite this article: Reshak, A. H. Spin-polarized Second Harmonic Generation from the Antiferromagnetic CaCoSO Single Crystal. *Sci. Rep.* **7**, 46415; doi: 10.1038/srep46415 (2017).

Publisher's note: Springer Nature remains neutral with regard to jurisdictional claims in published maps and institutional affiliations.